

# Swarm-Optimized ZnO/CdS/CIGS/GaAs Solar Cell for Enhanced Efficiency and Thermal Resilience

Habib Ullah Manzoor, Tareq Manzoor, Sajjad Hussain, Muhammad Nasir Manzoor, and Ahmed Zoha\*

Optimizing solar cell design is vital for boosting efficiency, cutting production costs, and meeting the increasing demand for renewable energy solutions. Through meticulous adjustments in material compositions and device architectures, optimization enhances energy conversion efficiency, making solar power more competitive and adaptable across various applications. This article presents the optimization and efficiency enhancement of a ZnO/CdS/CIGS solar cell with GaAs. The optimization process utilizes the particle swarm optimization algorithm with a step-by-step approach. Solar cells are designed using SCAPS-1D software, and optimization is performed using Python. The optimized ZnO/CdS/CIGS solar cell achieves an efficiency of 32.4%, which rises to 44.7% upon integrating a GaAs layer. Further efficiency gains are observed, reaching 53.2% through back contact optimization, providing a power density of  $54 \text{ mW cm}^{-2}$ . Optimization also notices a significant improvement in quantum efficiency. The cells are tested under concentrated solar irradiance ( $1000\text{--}10\,000 \text{ W m}^{-2}$ ) and temperatures (300–800 K). Results show that at  $10\,000 \text{ W m}^{-2}$  and 800 K, the ZnO/CdS/CIGS/GaAs cell requires 53.9% less material than the ZnO/CdS/CIGS cell. Thus, adding GaAs enhances efficiency and thermal resilience, making it ideal for concentrated photovoltaics.

## 1. Introduction

Amidst the current energy crisis, there has been significant attention given to finding feasible alternatives to hydrocarbons. Among these alternatives are solar, wind, and nuclear energy platforms. There has been growing interest in photovoltaic (PV) systems, such as solar cells, due to their various appealing features, including renewability, ease of installation, minimal pollution, and lack of noise.<sup>[1]</sup> Solar cells provide a pollution-free renewable energy source for generating electricity,<sup>[2]</sup> however, the issue of solar cell efficiency continues to be a topic of significant interest within the scientific community. Efficient photovoltaic cell development and integration encounter challenges primarily stemming from two key factors: efficiency and cost.

The cost of electricity is roughly ten times higher than the commercial prices of current solar cells.<sup>[3,4]</sup> Traditional solar panels, typically made from silicon crystal-

line wafer modules, tend to be bulky, complicating transportation. Enclosed within glass panels, these panels are essentially large-sized solar panels. Their bulky and heavy nature requires ample space, potentially large rooftops, for installation and support, especially for high-power applications. This drive for innovation in solar cell technology has resulted in notable advancements across three distinct generations: the first, second, and third generations of solar cells.<sup>[5]</sup> First-generation solar cells, made from monocrystalline and polycrystalline silicon, represented established technology but faced limited adoption due to their high manufacturing costs from complex processing methods. Conversely, second-generation solar cells, like commercially available CIGS-based solar cells, emerged as a more cost-effective alternative,<sup>[6]</sup> emerged with more affordable manufacturing processes. Third-generation solar cells, including organic/inorganic perovskite solar cells,<sup>[7–9]</sup> inorganic solar cells,<sup>[10,11]</sup> organic tandem solar cells,<sup>[12,13]</sup> quantum dot solar cells,<sup>[14–16]</sup> III-V solar cells,<sup>[17–20]</sup> and dye-sensitized solar cells (DSSCs),<sup>[21–23]</sup> represent a more complex and challenging manufacturing landscape to achieve desired results.

Power-generation systems can be optimized by selecting the right kind of solar cell technology according to your region,<sup>[24,25]</sup> increasing the conversion efficiency of photovoltaic systems,<sup>[26]</sup>

---

H. U. Manzoor, S. Hussain, A. Zoha  
James Watt School of Engineering  
University of Glasgow  
G12 8QQ, UK  
E-mail: Ahmed.Zoha@glasgow.ac.uk

H. U. Manzoor  
University of Engineering and Technology  
Lahore, Pakistan

T. Manzoor  
Energy Research Center  
COMSATS University Lahore  
Pakistan

M. N. Manzoor  
National Centre for Physics  
Pakistan

 The ORCID identification number(s) for the author(s) of this article can be found under <https://doi.org/10.1002/aesr.202400203>.

© 2024 The Author(s). Advanced Energy and Sustainability Research published by Wiley-VCH GmbH. This is an open access article under the terms of the Creative Commons Attribution License, which permits use, distribution and reproduction in any medium, provided the original work is properly cited.

DOI: [10.1002/aesr.202400203](https://doi.org/10.1002/aesr.202400203)

optimizing the tilt angle of solar cells,<sup>[27]</sup> efficiency optimization of layers in solar cells,<sup>[18,19]</sup> designing a power management system for optimal power usage,<sup>[28]</sup> opting to decentralized system,<sup>[29–33]</sup> using machine learning based anomaly detection system,<sup>[34–36]</sup> and leveraging concentrated sunlight.<sup>[37]</sup> Concentrating sunlight onto solar cells offers significant advantages, particularly in enhancing their efficiency and reducing production costs. Concentrated photovoltaic (CPV) systems can greatly enhance the intensity of solar radiation hitting the cells, hence increasing the cells' total efficiency, by focusing sunlight onto smaller areas of photovoltaic cells. This concentration also enables the use of high-efficiency materials like copper indium gallium selenide (CIGS), which have the potential to compete with traditional power-generation technologies.<sup>[38]</sup> With a bandgap of about 1.2 eV, CIGS-based solar cells are well-known for their great efficiency and comparatively cheap production costs. These cells can achieve greater open-circuit voltages and a lower temperature coefficient when exposed to concentrated sunlight, which can lead to notable improvements in performance and cost reductions.<sup>[39]</sup> This underscores the necessity for solar cells that excel under concentrated sunlight conditions.

In this research, we use a methodical, step-by-step strategy to optimize the thickness and carrier density of ZnO/CdS/CIGS solar cells, where ZnO serves as the antiglare layer. We achieve this by applying the particle swarm optimization (PSO) technique. Following the optimization of the ZnO/CdS/CIGS structure, we introduced a GaAs layer at the bottom and applied the PSO algorithm again to fine-tune its carrier density and thickness. Additionally, we refined the metal contact, which functions as the electrode.

We then subjected the optimized solar cell to concentrated sunlight and high temperatures. Our findings reveal that incorporating GaAs into the ZnO/CdS/CIGS solar cell not only boosts its efficiency but also enhances its ability to withstand high temperatures. This makes it particularly suitable for CPV applications, highlighting its potential for real-world implementation.

Following is the list of main contributions of this article: 1) This article presents the design and simulation of a ZnO/CdS/CIGS solar cell using SCAPS-1D software. The study models the physical and electrical characteristics of the solar cell structure to analyze its performance under various conditions. 2) We introduced a PSO algorithm specifically tailored to optimize the thickness and carrier density of solar cells. This algorithm is developed to enhance the efficiency and performance of the ZnO/CdS/CIGS solar cell. 3) Building upon the ZnO/CdS/CIGS solar cell design, we explored the integration of gallium arsenide (GaAs) into the structure. The PSO algorithm is then applied to optimize the incorporation of GaAs within the ZnO/CdS/CIGS solar cell, aiming to further improve its efficiency and performance. 4) We investigated the optimization of the back contact of the optimized ZnO/CdS/CIGS/GaAs solar cell. This involved refining the design of the electrical contact at the rear of the solar cell to minimize losses and maximize power output. 5) Finally, we evaluated the performance of the optimized ZnO/CdS/CIGS/GaAs solar cell under real-world conditions, specifically focusing on its response to concentrated sunlight and high temperatures. This analysis provides insights into the practical applicability and robustness of the optimized solar cell design.

## 2. Background

### 2.1. ZnO/CdS/CIGS Solar Cell

Recent research has significantly advanced the efficiency of CdS/CIGS solar cells, surpassing traditional efficiency standards.<sup>[40,41]</sup> The CIGS layer is notable for its flexibility and low weight, allowing it to be applied to various substrates. CIGS, a composite semiconductor material, contains precise amounts of gallium, indium, copper, and selenium.<sup>[42]</sup>

CIGS-based solar cells, utilizing the chalcopyrite structure, are highly promising due to their efficiency, affordability, and ease of integration.<sup>[43]</sup> These cells achieved a significant breakthrough with an efficiency of 22.6% using an absorber layer thickness of less than 2.5 μm.<sup>[44]</sup> Researchers are now exploring the use of this thin CIGS material in tandem cells, such as CIGS/CZTS, CIGS/Si, and Perovskite/CIGS, to leverage the advantages of thin-film technology.<sup>[45,46]</sup> The high-quality p-n junction formed between the CIGS and CdS layers plays a crucial role in the performance of these cells.<sup>[47]</sup>

The CdS buffer layer is essential for solar cells as it promotes the formation of the p-n junction and improves lattice coordination between the absorber and window layers. CdS, a type II-VI material, has a bandgap that varies with temperature and deposition conditions, typically ranging from 2.26 to 2.5 eV.<sup>[48,49]</sup>

Recent research has focused significantly on enhancing the efficiency of CdS/CIGS solar cells. For instance, incorporating a NiO hole transport layer has boosted the efficiency from 9.89% to 19.55%.<sup>[50]</sup> Another study achieved 22.25% efficiency by replacing the CdS buffer layer with ZnS.<sup>[51]</sup> The optimal thickness of the CdS layer for maximizing open-circuit voltage has been identified as 13 nm.<sup>[52]</sup> Further advancements include a CIGS solar cell model simulated with SCAPS-1D, which attained an open-circuit voltage,  $V_{oc}$  of 0.8975 V, a short-circuit current density,  $J_{sc}$  of 34.25 mA cm<sup>-2</sup>, a fill factor (FF) of 86.81%, and a power conversion efficiency,  $\eta$  of 26.68%, with a quantum efficiency of 98.86% at visible wavelengths.<sup>[53]</sup> Additionally, SCAPS-1D studies on bandgap grading profiles revealed efficiencies of 19.95% for linear grading and 21.10% for parabolic grading.<sup>[54]</sup> The Silvaco-Atlas two-dimensional device simulator has optimized Cu(In,Ga)Se<sup>2</sup> (CIGS) solar cells, increasing efficiency from 22.9% to 27.5% at room temperature and achieving a peak efficiency of 32.45% at 240 K.<sup>[55]</sup> Studies on minimizing absorber layer thickness and reducing heat losses demonstrated efficiencies of 17.1% with a graded CIGS structure, 19.0% with a ZnO<sub>0.5</sub>S<sub>0.5</sub> buffer layer, and 28.3% with a CIGS electron reflector layer.<sup>[56]</sup> Lastly, using Atlas Silvaco-TCAD tools, Cu(In<sub>1-x</sub>Ga<sub>x</sub>)Se<sup>2</sup> solar cells with a 1 μm thick absorber and MgF<sup>2</sup> antireflective coating achieved an efficiency of 25%, highlighting potential for ultrathin, flexible solar cell devices.<sup>[57]</sup> Further optimization involving layer thickness, Zn<sub>0.83</sub>Mg<sub>0.17</sub>O instead of ZnO, and the addition of a GaAs electron reflector and an extra CuInSe<sup>2</sup> absorber layer improved efficiency from 17% to 27.9%.<sup>[58]</sup>

### 2.2. GaAs Solar Cells

GaAs solar cells have been utilized in harsh environments, such as space applications, since their introduction in 1986.<sup>[59]</sup> They are renowned for their exceptional performance under extreme

conditions, making them a popular choice for aerospace and satellite applications. GaAs cells are highly resilient to radiation, exhibit high electron mobility, and possess a direct bandgap, making them particularly well-suited for space environments where exposure to cosmic rays and intense radiation levels is a significant concern.<sup>[60]</sup> Theoretical calculations suggest that the ideal bandgap energies for the top and bottom subcells of a tandem multijunction solar cell are  $\approx 1.65\text{--}1.8$  and  $1.0\text{--}1.5$  eV, respectively.<sup>[61]</sup> With a bandgap of around 1.43 eV, GaAs is within this optimal range, making it an ideal candidate for the bottom layer of multijunction solar cells designed for high-efficiency energy conversion.

GaAs solar cells offer numerous benefits that contribute to their widespread use in various applications:<sup>[62]</sup> 1) Improved photovoltaic conversion efficiency: GaAs exhibits higher efficiency compared to silicon solar cells, especially in low-light conditions or at elevated temperatures.<sup>[63]</sup> 2) Direct-gap semiconductor material: The direct bandgap of GaAs allows for efficient absorption of a broader range of the solar spectrum, resulting in higher conversion efficiencies compared to indirect bandgap semiconductors.<sup>[64]</sup> 3) Tailored bandgap characteristics:<sup>[65]</sup> The composition and doping of GaAs can be precisely controlled to tailor its bandgap, enabling optimization for optoelectronics, photovoltaics, and high-frequency devices. 4) Superior radiation resistance:<sup>[66]</sup> GaAs solar cells demonstrate exceptional resilience to radiation damage, ensuring reliable operation and longevity in harsh environments such as space.

These characteristics make GaAs solar cells a preferred choice for a wide range of applications, including space exploration, telecommunications, and terrestrial photovoltaic systems requiring high efficiency and durability.

### 2.3. CPV

CPV technology stands out as a top method for power production by concentrating sunlight. Additionally, CPV reduces the required area of photovoltaic cells, presenting a significant economic advantage.<sup>[67]</sup> The cost of solar cells can be reduced by using concentrated sunlight.<sup>[68]</sup> The different types of CPV systems include Fresnel lenses,<sup>[69]</sup> parabolic troughs,<sup>[70]</sup> dishes,<sup>[71]</sup> luminescent glass,<sup>[72]</sup> and compound parabolic concentrators.<sup>[73,74]</sup> CPV does not just increase incident of sunlight on the solar cell, it also increases its temperature as well. Wide-bandgap materials are indispensable for solar cells operating at high temperatures. This allows them to operate at much higher temperatures without significant degradation in performance.<sup>[75]</sup> The considerable bandgap exhibited by these materials necessitates higher energy input to transition electrons from the valence band to the conduction band. Consequently, they demonstrate reduced vulnerability to thermal excitation when exposed to elevated temperatures. This results in lower dark current and higher open-circuit voltages, which are crucial for efficient high-temperature solar cell operation.<sup>[75]</sup>

The materials we used in this work have bandgaps of 2.43, 1–2.5, and 1.43 eV for CdS, CIGS, and GaAs, respectively. These materials are all regarded as having a broad bandgap. A large portion of the sun spectrum can be absorbed by CIGS solar cells due to their high absorption coefficient.<sup>[76]</sup> This implies that even

in hot, sunny weather, they can produce power efficiently. Moreover, in comparison to other solar cell types, the temperature coefficient of CIGS cells is comparatively low.<sup>[77]</sup> Nevertheless, the thermal stability of CIGS-based solar cells is restricted, as breakdown mechanisms take place at temperatures higher than 350 °C.<sup>[78]</sup> The degradation of CIGS solar cells at high temperatures can be caused by various factors, including higher defect densities in the CIGS layer<sup>[79]</sup> and the establishment of an energy barrier for photogenerated electrons.<sup>[6]</sup> It has been demonstrated that the CdS buffer layer in CdS/CIGS solar cells gives the CIGS absorber layer more thermal stability and protection.<sup>[6,80,81]</sup>

As a result of its relatively high bandgap energy and capacity to continue operating at high temperatures, GaAs is a promising material for high-temperature solar cells.<sup>[82,83]</sup> Because GaAs has a wider bandgap than standard silicon solar cells, GaAs solar cells are recognized to have greater temperature stability.<sup>[84,85]</sup> Research has demonstrated that GaAs solar cells can operate at higher temperatures by maintaining higher power output and efficiency with hot energy carriers and at low lattice temperatures.<sup>[83,86,87]</sup> Given this, GaAs is a desirable option for CPV systems or solar cell applications in hot climates. In this work, we examine how power density affects concentrated sunlight on ZnO/CdS/CIGS and ZnO/CdS/CIGS/GaAs solar cells that have been constructed.

### 2.4. PSO Algorithm

The PSO algorithm takes inspiration from the collective behaviors observed in bird flocking and fish schooling. It operates as a population-based, stochastic optimization technique.<sup>[88]</sup> The process starts by setting up a group of potential solutions, referred to as particles, who explore the search area. Each particle has its own location and speed, which are adjusted during each round of the process.<sup>[89]</sup> One of the key benefits of using the PSO algorithm for optimizing solar cell parameters is its capability to handle nonlinear optimization problems efficiently. It is computationally effective and robust against varying initial conditions, making it an excellent choice for this purpose.<sup>[90]</sup> The PSO algorithm sees widespread usage in determining the parameters of solar cell models,<sup>[91]</sup> proving effective in extracting these parameters from illuminated current-voltage characteristics.<sup>[90]</sup> Numerous studies have applied the PSO technique to various types of solar cell models, including single-diode,<sup>[92]</sup> multijunction,<sup>[93]</sup> and more complex models with multiple diodes.<sup>[94]</sup> PSO-based algorithms have demonstrated better effectiveness when compared to alternative optimization methods, like genetic algorithms.<sup>[95]</sup> Table 1 lists the variables that will be discussed in the context of the PSO algorithm.

We wrote the code in Python using the following steps:

#### 1. Initialization

- 1) Set the dimensionality of the optimization landscape as  $\text{dim}$  and determine the number of particles in the swarm as  $n_p$ .
- 2) Generate random initial positions  $\text{pos}_i$  and velocities  $\text{vel}_i$  for each particle in the search space within a specified range.
- 3) Set each particle's personal best position  $p_{\text{best}}$  initially to its

**Table 1.** List of abbreviations.

Abbreviation	Description
dim	Dimensionality of the optimization landscape.
$n_p$	Amount of particles in the swarm.
$\text{pos}_i$	Position of particle $i$ in the optimization landscape.
$\text{vel}_i$	Velocity of particle $i$ in the optimization landscape.
$p_{\text{best}_i}$	Local optimal solution of particle $i$ .
$p_{\text{fit}_i}$	Fitness value corresponding to the local optimal solution of particle $i$ .
$g_{\text{best}}$	Global best position found by the swarm.
$g_{\text{fit}}$	Fitness value corresponding to the global best position found by the swarm.
$\text{max}_{\text{iter}}$	Maximum number of iterations.
$\text{fit}_i$	Fitness value of particle $i$ at its current position.
$\text{obj}_{\text{thickness}}$	Performance metric evaluating the fitness of a particle based on its position.
$\omega$	Inertia weight parameter controlling the particle's inertia.
$\phi_p$	Cognitive weight parameter determining the particle's cognitive influence.
$\phi_g$	Social weight parameter governing the particle's social influence.

current position and corresponding fitness  $p_{\text{fit}_i}$  to infinity. 4) Set the global best position  $g_{\text{best}}$  initially to none and its fitness  $g_{\text{fit}}$  to infinity. 5) Set the values of the inertia weight ( $\omega$ ), cognitive weight ( $\phi_p$ ), and social weight ( $\phi_g$ ) during initialization to regulate the influence of the particle's prior velocity, personal best position, and global best position on its movement, respectively.

## 2. Objective Function

1) Define the objective function, in this case, thickness of both materials  $\text{obj}_{\text{thickness}}$  to evaluate the fitness of a particle based on its position in the search space. 2) The objective function computes the fitness value by evaluating the efficiency of a solar cell with a given thickness.

## 3. Particle Movement

1) Iterate over a predefined number of iterations  $\text{max}_{\text{iter}}$ . 2) For each particle in the swarm: a) Assess the fitness  $\text{fit}_i$  of the particle's present position with objective function. b) Revise the particle's personal best position  $p_{\text{best}_i}$  and corresponding fitness  $p_{\text{fit}_i}$  if the current fitness surpasses its previous best. c) Adjust the global optimized position  $g_{\text{best}}$  and corresponding fitness  $g_{\text{fit}}$  if the current particle's fitness is superior to the global best. d) Modify the particle's velocity  $\text{vel}_i$  by integrating the inertia weight ( $\omega$ ), cognitive weight ( $\phi_p$ ), and social weight ( $\phi_g$ ), together with the local and global optimized positions. e) Update the particle's position  $\text{pos}_i$  by incorporating its velocity.

## 4. Termination

1) Continue iterating until a termination condition is satisfied, such as reaching the maximum number of iterations.

## 5. Result

1) The algorithm determines the global best position  $g_{\text{best}}$ , which represents the optimal solution discovered, and its related fitness  $g_{\text{fit}}$ , which denotes the performance of the photovoltaic

cell with the optimized thickness. 2) This PSO algorithm continually adjusts the positions of particles within the optimization landscape to converge toward the optimal solution, thereby maximizing the efficiency of the solar cell. By updating velocities based on personal and global best positions, particles effectively explore and exploit potential solutions within the optimization landscape.

## 3. Optimization Strategy

To improve the efficiency of solar cells by managing the thickness and carrier density of CdS and CIGS materials, we use a two-step method. Initially, we vary the thickness of each material relative to the other within the range of 0.5–5 µm. At each interval, we assess the solar cell efficiency ( $\eta$ ). Subsequently, leveraging the optimized thickness values, we adjust the doping density from  $1 \times 10^{10}$  to  $1 \times 10^{20}$  (cm $^{-3}$ ), re-evaluating  $\eta$ . These optimized  $\eta$  values, obtained from thickness and carrier density adjustments, serve as inputs for the PSO algorithm to derive the optimized parameters.

It is crucial to note that this optimization process unfolds sequentially rather than concurrently. Initially, we optimize the thickness parameters, followed by optimizing the carrier density parameters for the ZnO/CdS/CIGS solar cell. After optimizing the ZnO/CdS/CIGS solar cell, we introduce a GaAs solar layer at the bottom.

The GaAs layer thickness ranges from 0.5 to 5 µm, with doping density ranging from  $1 \times 10^{10}$  to  $1 \times 10^{20}$  (cm $^{-3}$ ). Efficiency calculations are carried out identically, and the PSO method is used to produce optimum parameters. This iterative process makes it easier to optimize thickness and carrier density across all layers of the solar cell construction. After optimizing the thickness and carrier densities for all layers, we optimize the back metal contact by introducing alternative metals into the optimized cell and observing  $\eta$ .

## 4. Simulation Setup

The figure presented in **Figure 1** illustrates a simple three-layered structured CdS/CIGS solar cell. It consists of a thin top layer of

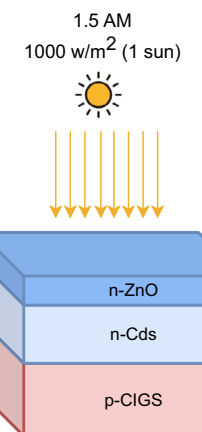


**Figure 1.** Schematic diagram of CdS/CIGS solar cell.

n-ZnO measuring  $0.01\text{ }\mu\text{m}$ , followed by layers of  $2\text{ }\mu\text{m}$  of p-CdS and p-CIGS. Both layers have a carrier density of  $1 \times 10^{15}$ . The values for the thickness and carrier density were initially chosen arbitrarily to establish a baseline for comparison with the optimized solar cell configurations. This baseline allows us to effectively evaluate the improvements achieved through the optimization process, as detailed in the subsequent sections of this manuscript. The parameters of the ZnO, CIGS, and CdS layers were obtained from ref. [96], while parameters for GaAs were obtained from ref. [97]. ZnO serves as a highly conductive n-type semiconductor, efficiently transporting electrons from the light-absorbing layer to the electrode. This attribute significantly amplifies the overall efficacy of charge collection within the solar cell.<sup>[98]</sup> Additionally, with its high refractive index, ZnO effectively functions as an antiglare coating on the solar cell. This feature diminishes light reflection and augments light absorption within the active layer.<sup>[99]</sup> Furthermore, ZnO can passivate the solar cell surface, mitigating the presence of recombination centers and consequently boosting both the  $V_{\text{oc}}$  and FF of the cell.<sup>[100]</sup>

We used the SCAPS-1D software<sup>[101]</sup> to perform simulations under standard scenarios of  $300\text{ K}$  temperature and  $1000\text{ W m}^{-2}$  incident sunlight (AM 1.5G). SCAPS, created by the Department of Electronic and Information Systems (ELIS) at the University of Gent, Belgium, is a well-known and standardized software platform for solar simulation studies.<sup>[101]</sup> The transport equation, the Poisson equation, and the continuity equation determine the behavior of carriers in solar devices. The carrier continuity equation is expressed as follows:

$$\frac{\partial P}{\partial t} = -\frac{1}{q} \nabla \cdot J_h - R + G \quad (1)$$

$$\frac{\partial N}{\partial t} = \frac{1}{q} \nabla \cdot J_e - R + G \quad (2)$$

In the provided equations,  $J_e$  and  $J_h$  represent the current density of electrons and holes, respectively, while  $R$  and  $G$  denote the rates of recombination and generation. The drift-diffusion equations for electrons and holes become:

$$J_e = qN(x)\mu_e \frac{dv(x)}{dx} - qD_e \frac{dN(x)}{dx} \quad (3)$$

$$J_h = qP(x)\mu_h \frac{dv(x)}{dx} - qD_h \frac{dP(x)}{dx} \quad (4)$$

here,  $\mu_h$  and  $\mu_e$  represent the mobility of holes and electrons, respectively, while  $D_e$  and  $D_h$  denote the diffusion constants for electrons and holes, respectively. The generation rates mentioned in the drift-diffusion equations are as follows:

$$G(\lambda, x) = \alpha\Phi(\lambda, x) \quad (5)$$

$$G = \int_{\lambda_{\min}}^{\lambda_{\max}} G(\lambda, x)d\lambda \quad (6)$$

here,  $\Phi(\lambda, x)$  represents the photon flux at position  $x$ ,  $\Phi_0(\lambda)$  denotes the photon flux at position  $x = 0$ ,  $T_f(\lambda)$  signifies the transmission of the front contact, and  $\alpha$  represents the absorption coefficient.  $G$  denotes the generation rates.

The Poisson equation becomes:

$$\nabla^2 V(x) = \frac{q}{\epsilon} [P(x) - N(x) + N_D - N_A] \quad (7)$$

where the electron charge is  $q$ , the permittivity of the absorber is  $\epsilon$ , the electrostatic potential is  $V(x)$ , the acceptor and donor dopant densities are  $N_A$  and  $N_D$ , respectively, and the position-dependent electron and hole concentrations are  $P(x)$  and  $N(x)$ .

The conversion efficiency ( $\eta$ ) of the designed solar cell is determined using the formula:

$$\eta = \frac{V_{\text{oc}} \cdot FF \cdot J_{\text{sc}}}{P_{\text{in}}} \quad (8)$$

here,  $V_{\text{oc}}$ ,  $J_{\text{sc}}$ , FF, and  $P_{\text{in}}$  denote the open-circuit voltage, short-circuit current density, fill factor, and input power, respectively. Quantum efficiency,  $\text{QE}(\lambda)$ , which measures the ratio of collected charge carriers to incident photons of a specific energy shining on the cell,<sup>[102]</sup> can be computed as:

$$\text{QE}(\lambda) = \frac{N_e(\lambda) + N_h(\lambda)}{N_{\gamma}(\lambda)} \times 100 \quad (9)$$

here,  $N_e(\lambda)$  and  $N_h(\lambda)$  denote the number of collected charge carriers, respectively, at wavelength  $\lambda$ , while  $N_{\gamma}(\lambda)$  represents the number of incoming photons at wavelength  $\lambda$ .

#### 4.1. Optimization of ZnO/Cds/CIGS Solar Cell

The unoptimized ZnO/CdS/CIGS solar cell provided  $V_{\text{oc}}$  of  $0.5\text{ V}$  and  $J_{\text{sc}}$  of  $40.5\text{ mA cm}^{-2}$  with FF of  $77.5\%$  and  $\eta$  of  $15.91\%$ . The IV and PV characteristics of the unoptimized ZnO/CdS/CIGS photovoltaic cell are plotted in Figure 2a, and Figure 2b shows the  $\text{QE}(\lambda)$ .  $\text{QE}(\lambda)$  is plotted from  $300$  to  $1200\text{ nm}$ . From  $300$  to  $500\text{ nm}$ , the  $\text{QE}(\lambda)$  remains at  $100\%$ ; further increase in wavelength to  $1130\text{ nm}$ , the  $\text{QE}(\lambda)$  starts to decrease nonlinearly toward zero.

##### 4.1.1. Thickness Optimization

We conducted calculations for  $\eta$  while varying the thickness of both CdS and CIGS layers from  $0.5$  to  $5\text{ }\mu\text{m}$ . The outcomes of this thickness variation are depicted in a 3D plot in Figure 3. It is evident that as the thickness of the CIGS material increases from  $0.5$  to  $5\text{ }\mu\text{m}$ ,  $\eta$  rises from  $16\%$  to  $20\%$ . Conversely, there is minimal variation observed in  $\eta$  with changes in the thickness of the CdS layer. This suggests that the optimization of thickness primarily hinges on the thickness of the CIGS layer.

A thicker CIGS layer can absorb more light, leading to a higher creation of charges, which are the charge carriers that contribute to the photocurrent and ultimately the conversion efficiency.<sup>[103]</sup> By increasing the thickness of the CIGS layer, a larger separation is achieved between the front and back contacts. This diminishes the likelihood of electron–hole recombination at the contacts, thereby enhancing the collection of charge carriers and ultimately improving  $\eta$ .<sup>[104,105]</sup> The increase in CIGS layer thickness generally improves the solar cell's conversion efficiency by enhancing light absorption, reducing recombination

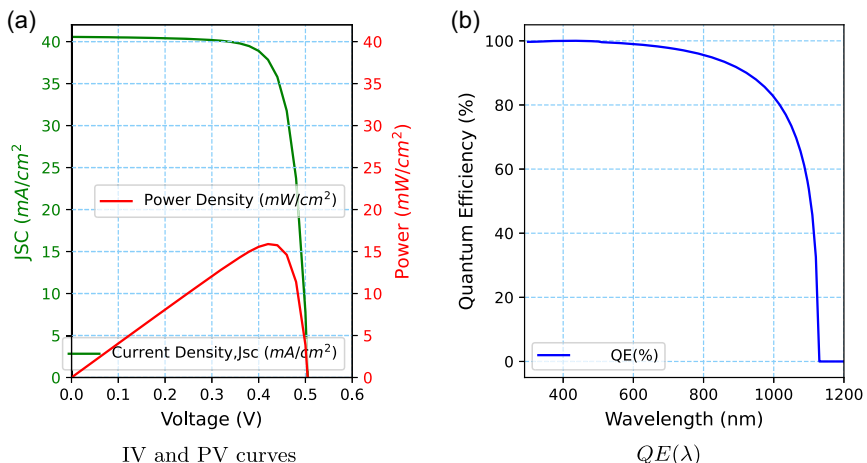


**Figure 2.** Unoptimized maps of CdS/CIGS solar cell. a) IV (green) and PV (red) curves, b) QE( $\lambda$ ).

losses, and optimizing the charge carrier generation and collection.<sup>[106,107]</sup>

The data plotted in Figure 3 is fed into the PSO algorithm to obtain optimized results. Based on our experiments of the PSO algorithm, the optimized thickness of CdS is 1  $\mu\text{m}$  and CIGS is 5  $\mu\text{m}$ . After thickness optimization, the achieved  $\eta$  is 20.1%.

#### 4.1.2. Carrier Density Optimization

Tailoring the carrier concentration profile in the CIGS and CdS layers can create a more favorable band alignment and minimize interface recombination.<sup>[108]</sup> To obtain the optimized doping density of both CdS and CIGS materials, we increased the doping density from  $10^{10}$  to  $10^{20}$   $\text{mA cm}^{-2}$ , keeping the optimized thickness constant, and observed the efficiency ( $\eta$ ). The effect of doping is plotted in Figure 4. The  $\eta$  is heavily influenced by the carrier densities of both layers.

As we increase the carrier density of CdS from  $10^{10}$  to  $10^{20}$   $\text{cm}^3$ ,  $\eta$  also increases linearly from 7% to 32.4% when CIGS has a carrier density of  $10^{20}$   $\text{mA cm}^{-2}$ . However, when the doping density of CIGS increases from  $10^{10}$  to  $10^{14}$   $\text{mA cm}^{-2}$  while the doping density of CdS is fixed at  $10^{20}$   $\text{cm}^3$ ,  $\eta$  remains the same at 23%, then suddenly increases to 30% as the doping density of CIGS increases from  $10^{14}$  to  $10^{16}$   $\text{cm}^3$ , and steadily rises to 32.4% for any further increase in the carrier density of the CIGS layer. These data are fed to the PSO algorithm, and an optimized carrier density of  $10^{20}$   $\text{cm}^3$  is obtained for both layers.

The IV and PV characteristics of the optimized ZnO/CdS/CIGS solar cell are plotted in Figure 5a, and Figure 5b shows the QE( $\lambda$ ). By comparing the results with Figure 2, it can be seen that after optimization,  $V_{oc}$  increased from 0.5 to 0.86 V,  $J_{sc}$  increased from 40.5 to 42.56  $\text{mA cm}^{-2}$ , FF increased from 77.5% to 86.92%, and  $\eta$  increased from 15.91% to 32.5%. The maximum achieved power density increased from 15.91% to

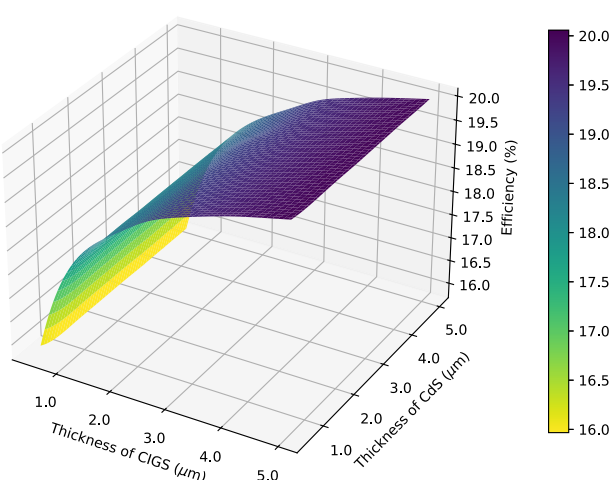


**Figure 3.** Relation between thickness of CdS and CIGS in ZnO/CdS/CIGS solar cell.

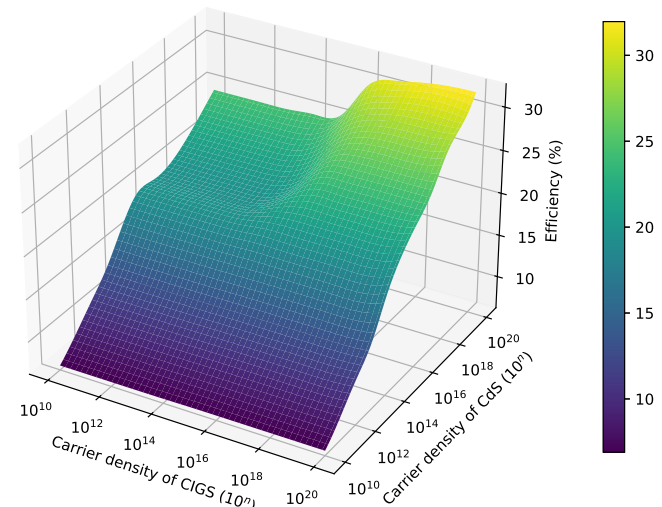


**Figure 4.** Relation between carrier density of CdS and CIGS in ZnO/CdS/CIGS solar cell.

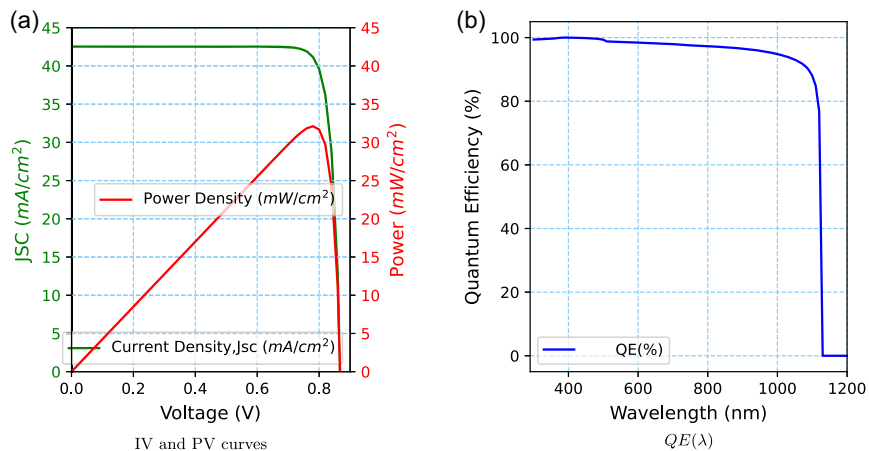


**Figure 5.** Optimized maps of CdS/CIGS solar cell. a) IV (green) and PV (red) curves, b) QE( $\lambda$ ).

32.4%, a 203.4% increase. The heightened carrier concentration within the CIGS absorber layer can lead to a larger built-in potential and enhanced charge separation, resulting in an increased  $V_{oc}$ .<sup>[109]</sup> Elevated carrier density strengthens the built-in electric field within the device, enhancing the separation and collection of charge carriers generated by light.<sup>[110]</sup> Furthermore, higher carrier densities have the potential to inhibit recombination, particularly at the ZnO/CIGS/CdS heterojunction.<sup>[111]</sup>

Optimizing the carrier density of CdS buffer layer and an absorber CIGS layer can improve the charge carrier separation and collection, leading to higher QE( $\lambda$ ).<sup>[109]</sup> Careful control of the carrier density and thickness can minimize recombination losses at the ZnO/CIGS/CdS interface, thereby enhancing the QE( $\lambda$ ).<sup>[112]</sup> A significant increase in QE( $\lambda$ ) is also observed, with 100% QE( $\lambda$ ) provided from 300 to 500 nm. Further increasing the wavelength to 1000 nm, QE( $\lambda$ ) decreases linearly to 95%, and then decreases nonlinearly toward zero when the wavelength is further increased to 1130 nm. Comparing Figure 2b and 5b, it can be inferred that by optimizing the CdS/CIGS solar cell, the slope of QE( $\lambda$ ) versus wavelength of incident light has improved. This improved QE( $\lambda$ ) within a solar cell leads to increased absorption of light and more efficient conversion of photons into electrical energy, resulting in higher overall efficiency and enhanced power output. By increasing the QE( $\lambda$ ), more of the incident solar radiation can be transformed into usable electrical energy.<sup>[113]</sup>

#### 4.2. Optimization of ZnO/CdS/CIGS/GaAs

Now, we added another layer at the bottom of ZnO/CdS/CIGS. The layer is made of p-GaAs, as presented in Figure 6. To optimize the newly added layer in the already optimized ZnO/CdS/CIGS solar cell, we varied the thickness of the GaAs layer from 0.5 to 5  $\mu$ m and the carrier density from  $10^{10}$  to  $10^{20}$  cm<sup>-3</sup>, observing the corresponding efficiency ( $\eta$ ). The effect of thickness and doping density of the GaAs layer on the ZnO/CdS/CIGS solar cell is plotted in Figure 7. We can observe a nonlinear correlation between thickness and doping density. From this, it can be deduced that thickness exerts a greater influence  $\eta$  than carrier density. As thickness increases, a significant increase in  $\eta$  is

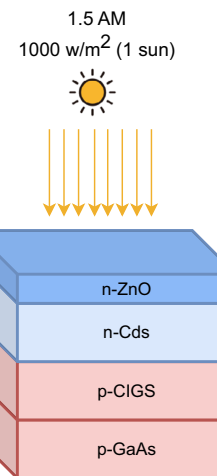


**Figure 6.** Schematic diagram of ZnO/ZnO/CdS/CIGS/GaAs solar cell.

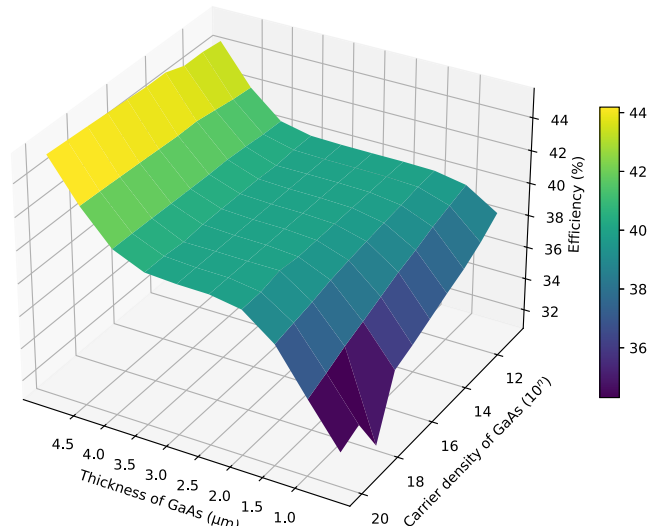


**Figure 7.** Relation between thickness and carrier density of GaAs in ZnO/CdS/CIGS/GaAs solar cell.

observed. However, the increase in carrier density at lower values of thickness, such as 0.5  $\mu\text{m}$ , had a higher impact on  $\eta$ , and the effect decreases as the values of thickness increase to 5  $\mu\text{m}$ . These results are fed to the PSO algorithm, and the optimized carrier density was  $10^{20} \text{ cm}^{-3}$  with a thickness of 5  $\mu\text{m}$ .

Enlarging the thickness of the GaAs absorber layer in solar cells has demonstrated an ability to enhance conversion efficiency.<sup>[114]</sup> Thicker absorber layers enable greater light absorption and the production of more electron–hole pairs, resulting in heightened photocurrent and efficiency.<sup>[114]</sup>

After optimization, the achieved  $\eta$  is 44.7%. The optimized IV, PV, and  $\text{QE}(\lambda)$  are plotted in **Figure 8**. Comparing with Figure 5, we can imply that  $V_{\text{oc}}$  increased from 0.86 to 1.2 V, however,  $J_{\text{sc}}$  remains almost unchanged. This is because GaAs has a higher bandgap. A higher bandgap allows for a higher  $V_{\text{oc}}$ , as the  $V_{\text{oc}}$  is closely tied to the bandgap energy of the semiconductor.<sup>[115,116]</sup> Furthermore, GaAs has lower recombination rates, which reduces the recombination current and increases  $V_{\text{oc}}$ .<sup>[117,118]</sup> Photon recycling is enhanced in GaAs solar cells, which boosts the  $V_{\text{oc}}$ .<sup>[119,120]</sup> Photon recycling occurs when photons emitted during radiative recombination are reabsorbed by the material, reducing net recombination losses. In GaAs solar cells, this process significantly boosts the open-circuit voltage ( $V_{\text{oc}}$ ) through several key mechanisms. When an electron recombines with a hole in GaAs, it emits a photon that can be reabsorbed by the material due to its high absorption coefficient.<sup>[121]</sup> This reabsorption extends the effective path length of photons within the cell, increasing the likelihood of generating additional electron–hole pairs.<sup>[122]</sup> Consequently, enhanced carrier generation contributes to a higher photocurrent.<sup>[123]</sup> Additionally, photon recycling minimizes radiative recombination losses by converting emitted photons into additional carriers instead of allowing them to escape or dissipate as heat.<sup>[124]</sup> This improved carrier generation and reduced recombination losses lead to a higher energy conversion efficiency, which directly increases  $V_{\text{oc}}$ . This enhancement results in an increase in efficiency ( $\eta$ ) from 32.4% to 44.6%, representing an 136% improvement in  $\eta$ . Although the GaAs layer is positioned at the bottom of the solar cell and does not significantly impact overall light absorption—especially since most absorption occurs in the CIGS layer, the primary

light-absorbing material—it is designed to improve other properties, such as band alignment or reducing recombination, without altering the total light absorption.<sup>[125,126]</sup> The optimized CdS/CIGS/GaAs solar cell achieves a power density of  $45.6 \text{ mW cm}^{-2}$ , with a quantum efficiency ( $\text{QE}(\lambda)$ ) of 100% across the spectrum from 300 to 1130 nm.

### 4.3. Effect of Back Metal Contact

Now that we have optimized the thickness and carrier densities of all the layers, we need to decide on the back metal contact, which will serve as the electrode. Electrodes can be optimized by changing the work function,  $\phi_m$ . The lowest energy needed to release an electron from a metal surface to a point immediately outside of it, usually into a vacuum, is known as the  $\phi_m$  of a metal. This is a basic metal property that is commonly expressed in electron volts (eV). Variations in the type of metal, its surface quality, and temperature can all affect the work function. It plays a crucial role in various physical phenomena, including electron emission processes like the photoelectric effect and thermionic emission, as well as in determining the behavior of metal–semiconductor junctions in electronic devices. In solar cell technology, the  $\phi_m$  of metal contacts holds crucial significance in extracting and collecting charge carriers. The metal contacts act as selective contacts, allowing the flow of desired charge carriers (either electrons or holes) while blocking the undesired ones.<sup>[98]</sup> This selective contact property is crucial for enhanced the  $\eta$  of photovoltaic cells.<sup>[127]</sup>

The work function of a metal can be measured as:

$$\phi_m = \psi + \kappa t \ln \left( \frac{D_V}{D_C} \right) \quad (10)$$

where  $\phi_m$  is the metal work function,  $\psi$  is the electron affinity,  $\kappa$  is the Boltzmann constant,  $t$  is the temperature,  $D_V$  is the valence band density of states, and  $D_C$  is the conduction band density of states. In this work, ten different metals were used. Their respective work functions were obtained from ref. [128]. By default, SCAPS-1D software used flat bands.

The effect of different metals as a back contact on  $\eta$  is plotted in **Figure 9**. This figure also shows corresponding  $\phi_m$  with their

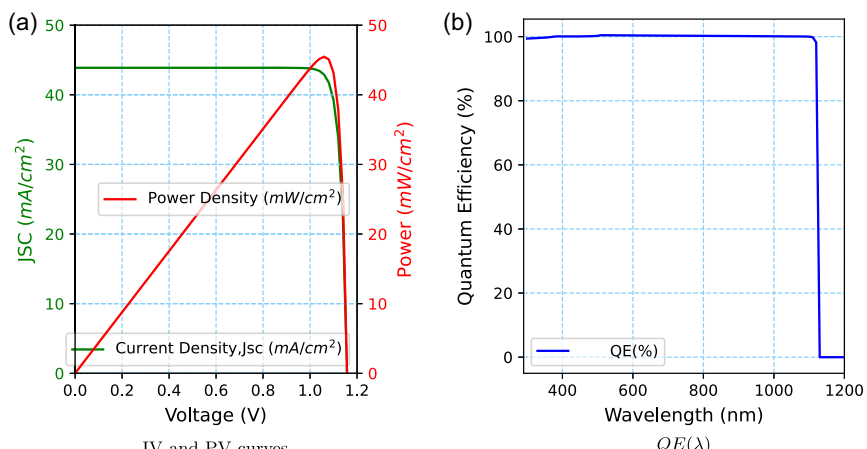


**Figure 8.** Optimized maps of ZnO/CdS/CIGS/GaAs solar cell. a) IV (green) and PV (red) curves, b)  $\text{QE}(\lambda)$ .

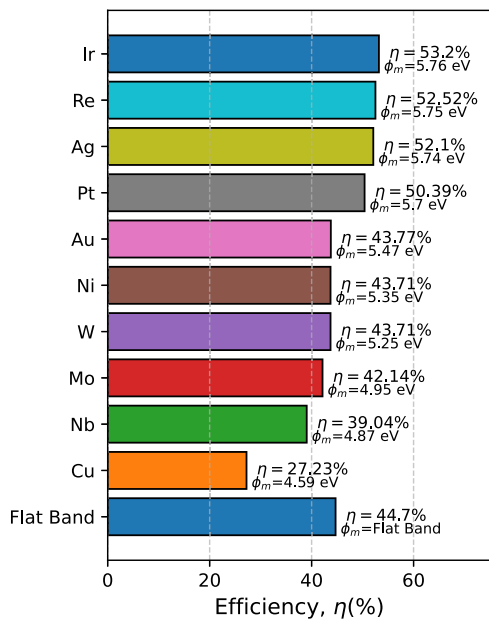


Figure 9. Effect of different work function on ZnO/CdS/CIGS/GaAs.

respective metals. It can be seen that  $\eta$  is directly proportional to  $\phi_m$ . This is because an improved  $\phi_m$  back contact improves the passivation and electron selectivity at the back interface, leading to better carrier collection and reduced recombination losses.<sup>[129]</sup> Furthermore, a higher  $\phi_m$  of back contact creates a better energy level alignment with the absorber layer, which facilitates charge extraction and suppresses recombination.<sup>[130]</sup> It can be noticed that the highest  $\eta$  of 53.2% was achieved with Ir and the lowest  $\eta$  of 27.23% with Cu metal. Ir has been investigated as a back contact material for solar cells due to its desirable properties.<sup>[131,132]</sup> It can be very effective at suppressing unwanted radiation and is resistant to oxidation, making it a suitable choice for solar cell applications.<sup>[131]</sup> It can help to eliminate the Schottky barrier and form an ohmic contact, which is important for improving the photovoltaic  $\eta$  of the device.<sup>[127]</sup>

#### 4.4. Results and Discussion

In our work, we designed a ZnO/CdS/CIGS/GaAs/Ir solar cell and optimized it using a sequentially designed strategy. The results of the optimized and unoptimized photovoltaic cells are plotted in Figure 10. A significant increase in power density is observed; the unoptimized CdS/CIGS provided a power density of  $15.91 \text{ mW cm}^{-2}$ , whereas the optimized ZnO/CdS/CIGS/GaAs/Ir solar cell provided  $54 \text{ mW cm}^{-2}$ , which is 3.6 times higher. Additionally, a substantial increase in  $\text{QE}(\lambda)$  is observed, with  $\text{QE}(\lambda)$  remaining at 100% throughout the spectrum of 300–1130 nm. A comprehensive comparative analysis is tabulated in Table 2, consisting of different CdS/CIGS-based solar cell  $\eta$  found in the literature. It can be concluded that our optimized solar cells provided much better  $\eta$  with relatively simpler structures. The CdS/CIGS solar cell provided  $\eta$  of 32.4%. Adding GaAs to CdS/CIGS increased the  $\eta$  to 44.62%. Further optimization of the back contact increased it to  $\eta$  of 53.2%.

#### 5. Effect of Concentrated Sunlight

When irradiance levels rise, more solar energy is incident upon the cell's surface, leading to an increase in absorbed energy.<sup>[133]</sup> This influx of energy can subsequently elevate the temperature of the solar cell. The phenomenon is particularly pronounced in concentrated sunlight scenarios, where focused solar radiation intensifies the energy absorbed by the cell, consequently raising its temperature. Hence, in this section, we varied incident solar irradiance from 1000 to  $10\,000 \text{ W m}^{-2}$  alongside temperature from 300 to 800 K and observed the power density of the CdS/CIGS and CdS/CIGS/GaAs solar cells. The effect of solar irradiance and temperature on CdS/CIGS and CdS/CIGS/GaAs is plotted in Figure 11 and 12, respectively. It can be implied that power density is directly proportional to solar irradiance. This is due to an increase in  $J_{sc}$  because the increased photon flux leads to the generation of more electron–hole pairs within the solar cell.<sup>[134]</sup>

It may be determined that power density falls with increasing temperature, owing to a rise in reverse saturation current and a drop in bandgap energy. The link between  $V_{oc}$  and reverse saturation current is expressed as follows in ref. [86]:

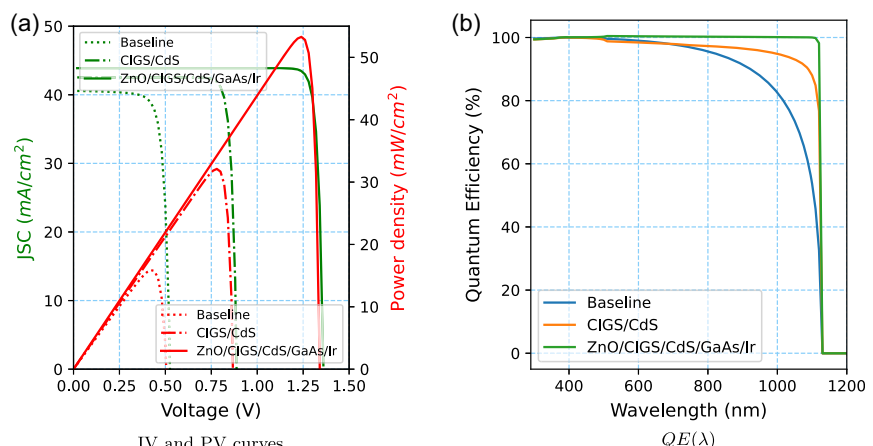


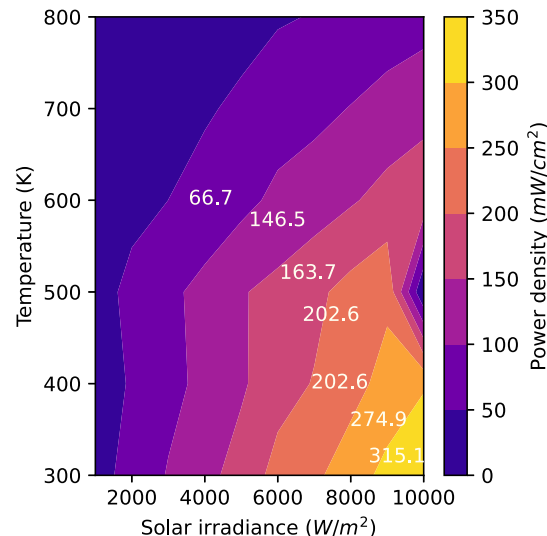
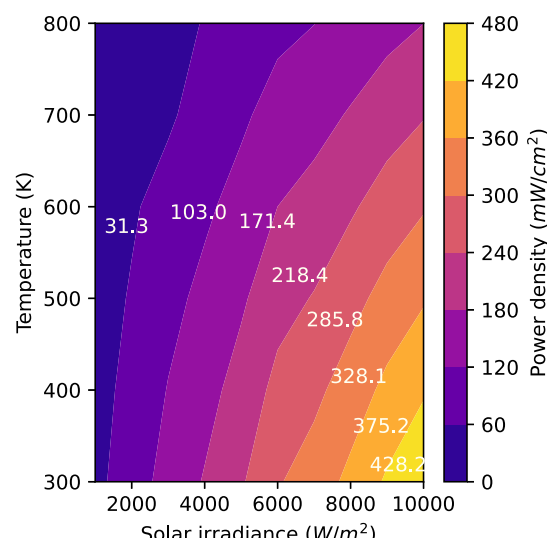
Figure 10. Comparison of unoptimised and optimised ZnO/CdS/CIGS/GaAs solar cell. a) IV (green) and PV (red) curves, b)  $\text{QE}(\lambda)$ .

**Table 2.** Efficiency of various solar cell structures and their references.

Serial no.	Solar cell structure	Efficiency [%]	References
1	Al:ZnO/CdS/CIGS/Mo	9.89	[50]
2	ZnO:B/i-ZnO/CdS/p + Layer/CIGS/Mo	17	[47]
3	CdS/CIGS	19.2	[112]
4	CdS/CIGS	19.2	[140]
5	Al:ZnO/CdS/CIGS/NiO/Mo	19.55	[50]
6	CdS/CIGS	19.62	[141]
7	CdS/CIGS	21.06	[142]
8	AZnO/ZnS/CIGS/Si/Mo	21.08	[143]
9	ZnO/CdS/Graded p-CIGS	21.1	[54]
10	ZnO/CdS/ZnS/CIGS/Mo	22.25	[51]
11	ZnO/CdS/Top CIGS/Bottom CIGS/Mo	22.3	[144]
12	AZO/ZnO/CdS/CIGS/CIGS/Mo	24.17	[145]
13	CdS/CIGS/PbS	24.22	[41]
14	Al-ZnO/i-ZnO/Zn(O,S)/CIGS/p-Si/Mo	24.43	[104]
15	Mo/CIGS/CdS/BTO/i-ZnO/AZO	24.45	[146]
16	ZnO:Al/i-ZnO/CdS/Cu(In <sub>1-x</sub> Ga <sub>x</sub> )Se <sup>2</sup>	24.5	[147]
17	Mo/CIGS/CdS/BTO/AZO	25.53	[146]
18	Mo/CIGS/CdS/i-ZnO/AZO	25.55	[146]
19	ZnO:Al/i-ZnO/CdS/CIGS/ER/MO	25.6	[148]
20	ZnO/CdS/CIGS/Mo	26.24	[149]
21	Al/ZnO:Al/i-ZnO/CdS/CIGS/Pt	26.68	[53]
22	ZnO/CdS/CIGS/MoS <sup>2</sup>	26.81	[150]
23	ZnO:Al/Zn <sub>0.83</sub> Mg <sub>0.17</sub> O/CdS/CIGS/GaAs/Mo	27.1	[58]
24	n-ZnO/i-ZnO/CdS/CIGS/Mo	27.48	[55]
25	CdS/CIGS	27.625	[151]
26	CdS/CIGS/m-Si/MoOx	28.08	[152]
27	ZnO:Al/Zn <sub>0.83</sub> Mg <sub>0.17</sub> O/ZnO <sub>0.5</sub> S <sub>0.5</sub> /Graded CIGS/CIGS/Mo	28.3	[56]
28	ZnO/CdS/CIGS	32.4	This work
29	SnO <sup>2</sup> /CdS/CIGS/BaS <sup>2</sup> /Mo	33.13	[149]
30	AZnO/CdS/CIGS/ZnO/CdS/CIGS/ZnO/CdS/CIGS/Mo	33.27	[153]
31	p-CGS/n-CGS/p-CIGS/n-CIGS	44.37	[154]
32	ZnO/CdS/CIGS/GaAs/Ir	53.2	This work

$$V_{oc}(T) = \frac{n k T_b}{q} \ln \left( \frac{J_{sc}}{J_0} + 1 \right) \quad (11)$$

here,  $n$ ,  $k$ ,  $T_b$ ,  $J_{sc}$ , and  $J_0$  represent the diode quantity factor, Boltzmann constant, current density, and reverse saturation current density. The solar cell's reverse saturation current grows exponentially with heat, combined with reduction in  $V_{oc}$ , results in a drop in both the FF and  $\eta$  of the device.<sup>[135]</sup> Furthermore, as the temperature increases, the bandgap energy of the solar cell material slightly decreases, leading to a small increase in the number of charge carriers produced.<sup>[135]</sup> This relation can be explained with Varshni's equation:<sup>[136]</sup>


**Figure 11.** Effect of concentrated sunlight with respect to temperature changes on power density on ZnO/CdS/CIGS solar cell.

**Figure 12.** Effect of concentrated sunlight with respect to temperature changes on power density on ZnO/CdS/CIGS/GaAs.

$$E_b(\theta) = E_b(0) - \frac{\gamma \theta^2}{\theta + \delta} \quad (12)$$

here,  $E_b(\theta)$  is the bandgap energy at temperature  $\theta$ ,  $E_b(0)$  is the bandgap energy at 0 K,  $\gamma$ , and  $\delta$  are material-specific Varshni parameters. The equation indicates a decrease in bandgap energy as temperature increases. The  $\gamma$  parameter determines the rate of decrease with temperature and the  $\delta$  parameter represents the temperature at which the  $E_b(\theta)$  reaches half its 0 K value.<sup>[137,138]</sup>

When comparing Figure 11 and 12, it is evident that ZnO/CdS/CIGS/GaAs exhibits a significantly higher power density than ZnO/CdS/CIGS solar cells. Moreover, the addition of GaAs to the ZnO/CdS/CIGS solar cell appears to mitigate the impact of increased temperature. The slope of ZnO/CdS/

CIGS/GaAs is notably steeper than that of ZnO/CdS/CIGS as the temperature rises from 300 to 800 K. This is due to the fact that GaAs has better thermal resistance. GaAs has a thermal conductivity of about  $0.55 \text{ W cm}^{-1} \text{ }^{\circ}\text{C}$ , which is roughly one-third that of silicon and one-tenth that of copper.<sup>[139]</sup> This lower thermal conductivity allows GaAs to retain heat more effectively, minimizing thermal gradients that could potentially lead to thermal runaway in devices. Additionally, the thermal diffusivity of GaAs, which measures how quickly heat spreads through the material, is about  $0.31 \text{ cm}^2 \text{ s}^{-1}$ .<sup>[139]</sup> This property ensures that temperature changes do not propagate quickly throughout the material, thereby helping to maintain stability within electronic components. The effect of increasing solar irradiance and temperature is almost linear in the ZnO/CdS/CIGS/GaAs solar cell, whereas in the ZnO/CdS/CIGS solar cell, a significant reduction in power density is observed after 500 K, moving toward 800 K. For instance, at  $6000 \text{ W m}^{-2}$  and 500 K, the ZnO/CdS/CIGS/GaAs cell exhibits a power density of  $\approx 218.386 \text{ mW cm}^{-2}$ , whereas the ZnO/CdS/CIGS cell shows a lower value of around  $146.460 \text{ mW cm}^{-2}$  which is 150% increase in power density. Since ZnO/CdS/CIGS/GaAs proved to have better power density, we can calculate the reduction in material requirement to generate the same amount of power density by the CdS/CIGS solar cell by using:

$$x = 1 - \frac{\text{Power density of ZnO/CdS/CIGS}}{\text{Power density of ZnO/CdS/CIGS/GaAs}} \quad (13)$$

here,  $x$  represents the reduction in material. At a temperature of 800 K and solar irradiance of  $10000 \text{ W m}^{-2}$ ,  $\approx 53.9\%$  less material would be required for the ZnO/CdS/CIGS/GaAs solar cell to produce the same power density.

However, the improvement in high-temperature performance comes at the cost of increased complexity and manufacturing challenges for GaAs-based solar cells.<sup>[63]</sup>

## 6. Conclusion

This study underscores the significance of optimizing solar cells to meet the escalating demand for renewable energy solutions. Through meticulous adjustments in material compositions and device architectures, substantial enhancements in energy conversion efficiency and cost reduction are attainable. The optimization and efficiency enhancement of a ZnO/CdS/CIGS solar cell with GaAs, employing the PSO algorithm, yielded noteworthy results. The optimized solar cell showcased an efficiency increase from 32.4% to 53.2%, with the integration of a GaAs layer and subsequent back contact optimization, achieving a power density of  $54 \text{ mW cm}^{-2}$ . Furthermore, testing under concentrated incident solar irradiance ranging from 1000 to  $10000 \text{ W m}^{-2}$  and temperatures spanning from 300 to 800 K unveiled that the ZnO/CdS/CIGS/GaAs solar cell required a staggering 53.9% less material compared to its counterpart, while maintaining high efficiency levels. Overall, the addition of GaAs not only bolstered efficiency but also bolstered the cell's durability under challenging environmental conditions, rendering it a compelling choice for CPV applications.

## Acknowledgements

The authors would like to extend their acknowledgment to Gent University, Belgium, for developing and providing the SCAPS-1D simulator used in this work.

## Conflict of Interest

The authors declare no conflict of interest.

## Author Contributions

**Habib Ullah Manzoor:** Conceptualization, data curation, formal analysis, methodology, software, and writing—original draft. **Naisir Manzoor:** Software, formal analysis, and data curation. **Sajjad Hussain:** Supervision, resources, validation, and writing—review and editing. **Tariq Manzoor:** Conceptualization, investigation, and formal analysis. **Ahmed Zoha:** Resources, supervision, project administration, validation, and writing—review and editing.

## Data Availability Statement

Data sharing is not applicable to this article as no new data were created or analyzed in this study.

## Keywords

concentrated photovoltaics, efficiency, GaAs, partial swarm optimization, solar cells

Received: July 8, 2024

Revised: August 8, 2024

Published online: September 23, 2024

- [1] S. Ghosh, R. Yadav, *Sustainable Energy Technol. Assess.* **2021**, 47, 101410.
- [2] J. Haque, Z. Islam, A. S. R. Ayon, A. Jabed, Z. R. Shaitee, S. T. Proma, E. Begum, M. H. Kabir, M. M. Ali, M. A. Kaiyum, *Sustainable Nanomaterials for Biosystems Engineering*, Apple Academic Press, Milton Park, Oxfordshire, **2023**, pp. 3–25.
- [3] P. Verlinden, *J. Renewable Sustainable Energy* **2020**, 12, 5.
- [4] B. M. Squeo, L. Ganzer, T. Virgili, M. Pasini, *Molecules* **2020**, 26, 153.
- [5] B. P. Singh, S. K. Goyal, P. Kumar, *Mater. Today: Proc.* **2021**, 43, 2843.
- [6] B. Salhi, *Materials* **2022**, 15, 1908.
- [7] J. J. Yoo, G. Seo, M. R. Chua, T. G. Park, Y. Lu, F. Rotermund, Y.-K. Kim, C. S. Moon, N. J. Jeon, J.-P. Correa-Baena, B. Vladimir, S. S. Seong, G. B. Moungi, S. Jangwon, *Nature* **2021**, 590, 587.
- [8] T. Wu, Z. Qin, Y. Wang, Y. Wu, W. Chen, S. Zhang, M. Cai, S. Dai, J. Zhang, J. Liu, Z. Zhou, X. Liu, H. Segawa, H. Tan, Q. Tang, J. Fang, Y. Li, L. Ding, Z. Ning, Y. Qi, Y. Zhang, L. Han, *Nano-Micro Lett.* **2021**, 13, 152.
- [9] N. S. Kumar, K. C. B. Naidu, *J. Materomics* **2021**, 7, 940.
- [10] W. Xiang, S. Liu, W. Tress, *Angew. Chem.* **2021**, 133, 26644.
- [11] X. Liu, H. Lian, Z. Zhou, C. Zou, J. Xie, F. Zhang, H. Yuan, S. Yang, Y. Hou, H. G. Yang, *Adv. Energy Mater.* **2022**, 12, 2103933.
- [12] F. Ullah, C.-C. Chen, W. C. Choy, *Adv. Energy Sustainability Res.* **2021**, 2, 2000050.
- [13] X. Wang, D. Zhang, B. Liu, X. Wu, X. Jiang, S. Zhang, Y. Wang, D. Gao, L. Wang, H. Wang, Z. Huang, X. Xie, T. Chen, Z. Xiao, Q. He, S. Xiao, Z. Zhu, S. Yang, *Adv. Mater.* **2023**, 35, 2305946.

- [14] M. Albaladejo-Siguan, E. C. Baird, D. Becker-Koch, Y. Li, A. L. Rogach, Y. Vaynzof, *Adv. Energy Mater.* **2021**, *11*, 2003457.
- [15] G. S. Selopal, H. Zhao, Z. M. Wang, F. Rosei, *Adv. Funct. Mater.* **2020**, *30*, 1908762.
- [16] Q. Zhao, R. Han, A. R. Marshall, S. Wang, B. M. Wieliczka, J. Ni, J. Zhang, J. Yuan, J. M. Luther, A. Hazarika, G.-R. Li, *Adv. Mater.* **2022**, *34*, 2107888.
- [17] A. Tan, H. U. Manzoor, N. Hamzah, M. Ahmad, S. Ng, Z. Hassan, *Optik* **2022**, *271*, 170095.
- [18] H. U. Manzoor, T. Kwan, N. Shiong, Z. Hassan, *Sains Malaysiana* **2022**, *51*, 1567.
- [19] H. Manzoor, M. M. Zawawi, M. Pakhuruddin, S. Ng, Z. Hassan, *Phys. B: Condens. Matter* **2021**, *622*, 413339.
- [20] H. U. Manzoor, S. Manzoor, M. A. Jamshed, T. Manzoor, *IET Networks* **2024**.
- [21] A. S. Najm, S. A. Alwash, N. H. Sulaiman, M. Chowdhury, K. Techato, *Environ. Prog. Sustainable Energy* **2023**, *42*, e13955.
- [22] F. Grifoni, M. Bonomo, W. Nairn, N. Barbero, T. Alnasser, I. Dzeba, M. Giordano, A. Tsaturyan, M. Urbani, T. Torres, C. Barolo, F. Sauvage, *Adv. Energy Mater.* **2021**, *11*, 2101598.
- [23] X. Hou, K. Aitola, P. D. Lund, *Energy Sci. Eng.* **2021**, *9*, 921.
- [24] U. Farooq, H. U. Manzoor, A. Mehmood, A. Iqbal, R. Younis, A. Iqbal, F. Yang, M. A. S. Hassan, N. Faiz, *Int. J. Adv. Comput. Sci. Appl.* **2019**, *10*, 5.
- [25] R. Younis, A. Iqbal, U. Farooq, A. Iqbal, H. U. Manzoor, A. Mehmood, T. Manzoor, in *2018 Int. Conf. on Power Generation Systems and Renewable Energy Technologies (PGSRET)*, IEEE , Islamabad **2018**, pp. 1–5.
- [26] Z. U. Abideen, A. Aslam, H. U. Manzoor, T. Manzoor, N. Bashir, in *2019 Int. Conf. on Electrical, Communication, and Computer Engineering (ICECCE)*, IEEE, Swat **2019**, pp. 1–5.
- [27] M. W. Ashraf, S. M. Aaqib, H. U. Manzoor, M. W. Ashraf, T. Manzor, M. H. Sethi, in *2020 IEEE 23rd Int. Multitopic Conf. (INMIC)*, IEEE, Bahawalpur **2020**, pp. 1–5.
- [28] H. U. Manzoor, A. R. Khan, M. Al-Quraan, L. Mohjazi, A. Taha, H. Abbas, S. Hussain, M. A. Imran, A. Zoha, in *2022 4th Global Power, Energy and Communication Conf. (GPECOM)*, IEEE, Türkiye **2022**, pp. 644–649.
- [29] H. U. Manzoor, S. Hussain, D. Flynn, A. Zoha, *TechRxiv*, Submitted: June **2024**. <https://doi.org/10.36227/techrxiv.171779422.29509780/v1>.
- [30] H. U. Manzoor, A. R. Khan, D. Flynn, M. M. Alarm, M. Akram, M. A. Imran, A. Zoha, *Sensors* **2023**, *23*, 3570.
- [31] A. Shabbir, H. U. Manzoor, R. A. Ahmed, Z. Halim, in *2024 Int. Conf. on Green Energy, Computing and Sustainable Technology (GECOST)*, IEEE, Miri Sarawak **2024**, pp. 245–249.
- [32] H. U. Manzoor, K. Arshad, K. Assaleh, A. Zoha, *TechRxiv*, Submitted: May **2024**. <https://doi.org/10.36227/techrxiv.171468119.91309905/v1>.
- [33] H. U. Manzoor, A. Jafri, A. Zoha , *TechRxiv*, Submitted: June **2024**. <https://doi.org/10.36227/techrxiv.171941779.95147304/v1>.
- [34] A. Basit, H. U. Manzoor, M. Akram, H. E. Gelani, S. Hussain, *J. Eng.* **2024**, *2024*, e12405.
- [35] H. U. Manzoor, M. S. Khan, A. R. Khan, F. Ayaz, D. Flynn, M. A. Imran, A. Zoha, in *2022 29th IEEE Int. Conf. on Electronics, Circuits and Systems (ICECS)*, IEEE, Glasgow **2022**, pp. 1–4.
- [36] H. U. Manzoor, A. R. Khan, T. Sher, W. Ahmad, A. Zoha, in *2023 IEEE 34th Annual Int. Symp. on Personal, Indoor and Mobile Radio Communications (PIMRC)*, IEEE, Toronto, ON **2023**, pp. 1–6.
- [37] K. Shanks, S. Senthilarasu, T. K. Mallick, *Renewable Sustainable Energy Rev.* **2016**, *60*, 394.
- [38] I. M. Alarifi, *Mater. Today: Proc.* **2023**, *81*, 403.
- [39] S.-I. Na, Y.-H. Seo, Y.-C. Nah, S.-S. Kim, H. Heo, J.-E. Kim, N. Rolston, R. H. Dauskardt, M. Gao, Y. Lee, D. Vak, *Adv. Funct. Mater.* **2019**, *29*, 1805825.
- [40] A. Gavrik, A. L. Mannanov, S. Tsarev, V. V. Bruevich, V. A. Trukhanov, Y. A. Chernikov, P. S. Savchenko, J. D. Gvozdikova, A. N. Solodukhin, P. A. Troshin, S. A. Ponomarenko, D. Y. Paraschuk, *Sol. Energy* **2020**, *206*, 770.
- [41] B. Barman, P. Kalita, *Sol. Energy* **2021**, *216*, 329.
- [42] J. Kim, C. Park, S. Pawar, A. I. Inamdar, Y. Jo, J. Han, J. Hong, Y. S. Park, D.-Y. Kim, W. Jung, H. Kim, H. Im, *Thin Solid Films* **2014**, *566*, 88.
- [43] Y. B. M. Yusoff, *Comprehensive Guide on Organic and Inorganic Solar Cells*, Elsevier, Amsterdam, **2022**, pp. 85–113.
- [44] N. E. I. Boukortt, *Optik* **2019**, *185*, 707.
- [45] N.-G. Park, *Trans. Electr. Electron. Mater.* **2020**, *21*, 1.
- [46] M. Al-Hattab, E. Oublal, M. Sahal, O. Bajjou, K. Rahmani , *Sol. Energy* **2022**, *248*, 221.
- [47] N. Guirdjebaye, A. T. Ngoupo, S. Ouédraogo, G. M. Tcheum, J. Ndjaka, *Chin. J. Phys.* **2020**, *67*, 230.
- [48] A. Quattropani, D. Stoeffler, T. Fix, G. Schmerber, M. Lenertz, G. Versini, J. Rehspringer, A. Slaoui, A. Dinia, S. Colis, *J. Phys. Chem. C* **2018**, *122*, 1070.
- [49] N. Brihi, F. Lmai, Z. Takkouk, F. Ayad, M. Ayoub, M. Hage-Ali, *Mater. Sci. Eng.: B* **2007**, *137*, 49.
- [50] T. Chargui, F. Lmai, A.-H. Mohamed, O. Bajjou, K. Rahmani, *Opt. Mater.* **2023**, *140*, 113849.
- [51] H. I. Abdalmageed, M. Fedawy, M. H. Aly, *J. Phys.: Conf. Ser.* **2021**, *2128*, 012009.
- [52] K. S. Cho, J. Jang, J.-H. Park, D.-K. Lee, S. Song, K. Kim, Y.-J. Eo, J. H. Yun, J. Gwak, C.-H. Chung, *ACS Omega* **2020**, *5*, 23983.
- [53] M. S. Uddin, R. Hosen, S. Sikder, H. Mamur, M. R. A. Bhuiyan, *Next Energy* **2024**, *2*, 100080.
- [54] S. Rawat, R. Gupta, S. Gohri, *Mater. Today: Proc.* **2023**. <https://www.sciencedirect.com/science/article/pii/S2214785323014025>.
- [55] M. W. Bouabdelli, F. Rogti, M. Maache, A. Rabehi, *Optik* **2020**, *216*, 164948.
- [56] S. R. F. S. Panahi, A. Abbasi, V. Ghods, M. Amirahmadi, *J. Mater. Sci.: Mater. Electron.* **2021**, *32*, 2041.
- [57] N. E. I. Boukortt, S. Patanè, Y. M. Abdulraheem, *Sol. Energy* **2020**, *204*, 440.
- [58] S. R. Fatemi Sharif Panahi, A. Abbasi, V. Ghods, M. Amirahmadi, *J. Mater. Sci.: Mater. Electron.* **2020**, *31*, 11527.
- [59] P. Bouisset, V. Nguyen, Y. Akatov, M. Siegrist, N. Parmentier, V. Archangelsky, A. Vorotsov, V. Petrov, E. Kovalev, *Adv. Space Res.* **1992**, *12*, 363.
- [60] E. D. Palik, *Handbook of Optical Constants of Solids*, Elsevier, Amsterdam, **1997**, pp. 429–443.
- [61] V. M. Andreev, *Practical Handbook of Photovoltaics*, Elsevier, Amsterdam, **2003**, pp. 417–433.
- [62] R. R. King, C. M. Fetzer, P. C. Colter, K. M. Edmondson, J. H. Ermer, H. L. Cotal, H. Yoon, A. P. Stavrides, G. Kinsey, D. D. Krut, N. H. Karam in *Conf. Record of the Twenty-Ninth IEEE Photovoltaic Specialists Conf.*, 2002, IEEE, New Orleans, LA **2002**, pp. 776–781.
- [63] W.-W. Zhang, H. Qi, Y.-K. Ji, M.-J. He, Y.-T. Ren, Y. Li, *Sol. Energy* **2021**, *230*, 1122.
- [64] A. A. Abushattal, A. G. Loureiro, N. E. I. Boukortt, *Micromachines* **2024**, *15*, 204.
- [65] A. Ali, A. W. Anwar, M. Moin, M. Babar, U. Thumu, *Heliyon* **2024**, *10*, 2.
- [66] T. Wang, Z. Wang, S. Zhang, A. Aierken, B. Wang, L. Fang, Y. Zhuang, M. Li, G. Tang, *Mater. Sci. Semicond. Process.* **2023**, *163*, 107562.
- [67] A. Ejaz, H. Babar, H. M. Ali, F. Jamil, M. M. Janjua, I. R. Fattah, Z. Said, C. Li, *Sustainable Energy Technol. Assess.* **2021**, *46*, 101199.

- [68] I. Ogunleye, O. Awogbemi, *Am. J. Sci. Ind. Res.* **2011**, 2, 11.
- [69] W. Xie, Y. Dai, R. Wang, K. Sumathy, *Renewable Sustainable Energy Rev.* **2011**, 15, 2588.
- [70] D. Krüger, Y. Pandian, K. Hennecke, M. Schmitz, *Desalination* **2008**, 220, 612.
- [71] G. Mittelman, A. Kribus, O. Mouchtar, A. Dayan, *Sol. Energy* **2009**, 83, 1322.
- [72] W. G. Van Sark, K. W. Barnham, L. H. Slooff, A. J. Chatten, A. Büchermann, A. Meyer, S. J. McCormack, R. Koole, D. J. Farrell, R. Bose, E. E. Berde, A. R. Burgers, T. Budel, J. Quilitz, M. Kennedy, T. Meyer, C. De Mello Donegá, A. Meijerink, D. Vanmaekelbergh, *Opt. Express* **2008**, 16, 21773.
- [73] T. K. Mallick, P. C. Eames, *Sol. Energy Mater. Sol. Cells* **2007**, 91, 597.
- [74] T. K. Mallick, P. C. Eames, B. Norton, *Sol. Energy* **2006**, 80, 834.
- [75] J. B. Varley, B. Shen, M. Higashiwaki, *J. Appl. Phys.* **2022**, 131, 23.
- [76] N. L. F. Chamidah, N. Mutfi, A. S. Dewi, A. A. Permanasari, S. Sunaryono, in *E3S Web of Conf.*, Vol. 473, EDP Sciences, Denpasar **2024**, p. 01004.
- [77] L. Lin, N. Ravindra, *SN Appl. Sci.* **2020**, 2, 1361.
- [78] T. G. Bontrager, S. Karthikeyan, S. Hwang, M. J. Sibakoti, B. T. Benton, S. A. Campbell, *IEEE J. Photovoltaics* **2019**, 10, 267.
- [79] S. Karthikeyan, S. Hwang, M. Sibakoti, T. Bontrager, R. W. Liptak, S. A. Campbell, *Appl. Surf. Sci.* **2019**, 493, 105.
- [80] A. Ferouani, M. M. Boudia, A. Cheknane, B. Benyoucef, *J. Fundam. Appl. Sci.* **2011**, 3, 77.
- [81] M. Fathi, M. Abderrezek, F. Djahli, M. Ayad, *Energy Procedia* **2015**, 74, 1410.
- [82] E. E. Perl, J. Simon, D. J. Friedman, N. Jain, P. Sharps, C. McPheeetters, Y. Sun, M. L. Lee, M. A. Steiner, *IEEE J. Photovoltaics* **2018**, 8, 640.
- [83] A. Maros, S. Gangam, Y. Fang, J. Smith, D. Vasileska, S. Goodnick, M. I. Bertoni, C. B. Honsberg, in *2015 IEEE 42nd Photovoltaic Specialist Conf. (PVSC)*, IEEE, New Orleans, LA **2015**, pp. 1–5.
- [84] N. Papež, R. Dallaev, S. Tälu, J. Kaštýl, *Materials* **2021**, 14, 3075.
- [85] C. F. Kamdem, A. T. Ngoupo, F. X. A. Abega, A. M. N. Abena, J.-M. B. Ndjaka, *Int. J. Photoenergy* **2023**, 2023. <https://onlinelibrary.wiley.com/doi/full/10.1155/2023/6204891>.
- [86] P. Singh, N. M. Ravindra, *Sol. Energy Mater. Sol. Cells* **2012**, 101, 36.
- [87] A. Belghachi, A. Helmaoui, A. Cheknane, *Progress in Photovoltaics: Research and Applications* **2010**, 18, 79.
- [88] A. G. Gad, *Arch. Comput. Methods Eng.* **2022**, 29, 2531.
- [89] A. P. Engelbrecht, *Computational Intelligence: An introduction*, John Wiley & Sons, Hoboken, NJ **2007**.
- [90] S. M. Ebrahimi, E. Salahshour, M. Malekzadeh, F. Gordillo, *Energy* **2019**, 179, 358.
- [91] D. B. Hmamou, M. Elyaqouti, E. Arjdal, J. Chaoufi, D. Saadaoui, S. Lidaighbi, R. Aqel, *Mater. Today: Proc.* **2022**, 52, 7.
- [92] N. F. A. Hamid, N. A. Rahim, J. Selvaraj, in *2013 IEEE Conf. on Clean Energy and Technology (CEAT)*, IEEE, Langkawi **2013**, pp. 461–465.
- [93] K. Ishaque, Z. Salam, A. Shamsudin, in *IECON 2011-37th Annual Conf. of the IEEE Industrial Electronics Society*, IEEE, Melbourne, VIC **2011**, pp. 1214–1219.
- [94] M. K. Singla, J. Gupta, M. H. Alsharif, M.-K. Kim, *PLoS One* **2024**, 19, e0296800.
- [95] A. Elsheikh, M. Abd Elaziz, *Int. J. Environ. Sci. Technol.* **2019**, 16, 1159.
- [96] H. Heriche, Z. Rouabah, N. Bouarissa, *Int. J. Hydrogen Energy* **2017**, 42, 9524.
- [97] A. Nassour, M. Kandouci, A. Belghachi, in *Int. Conf. on Electrical Engineering and Control Applications*, Springer, Constantine **2017**, pp. 304–313.
- [98] C. Thu, P. Ehrenreich, K. K. Wong, E. Zimmermann, J. Dorman, W. Wang, A. Fakharuddin, M. Putnik, C. Drivas, A. Koutsoubelitis, M. Vasilopoulou, L. C. Palilis, S. Kennou, J. Kalb, T. Pfadler, L. Schmidt-Mende, *Sci. Rep.* **2018**, 8, 3559.
- [99] Y.-J. Lee, D. S. Ruby, D. W. Peters, B. B. McKenzie, J. W. Hsu, *Nano Lett.* **2008**, 8, 1501.
- [100] Y. Han, J. Guo, Q. Luo, C.-Q. Ma, *Adv. Energy Sustainability Res.* **2023**, 4, 2200179.
- [101] M. Burgelman, P. Nollet, S. Degrave, *Thin Solid Films* **2000**, 361, 527.
- [102] M. Kaya, S. Hajimirza, *Sci. Rep.* **2018**, 8, 1.
- [103] M. F. Rahman, M. Chowdhury, L. Marasamy, M. K. Mohammed, M. D. Haque, S. R. Al Ahmed, A. Irfan, A. R. Chaudhry, S. Goumri-Said, *RSC Adv.* **2024**, 14, 1924.
- [104] M. Chadel, A. Chadel, B. Benyoucef, M. Aillerie, *Energies* **2023**, 16, 2956.
- [105] L. Chen, C. Fang, W. Liu, in *IOP Conf. Series: Earth and Environmental Science*, Vol. 440, IOP Publishing, Warith Al-Anbiya University, Karbala **2020**, p. 032051.
- [106] L. M. Mansfield, A. Kanevce, S. P. Harvey, K. Bowers, C. Beall, S. Glynn, I. L. Repins, *Progr. Photovoltaics: Res. Appl.* **2018**, 26, 949.
- [107] H. Kim, D. Xu, *Adv. Mater. Phys. Chem.* **2022**, 12, 195.
- [108] M. Gloeckler, J. Sites, *Thin Solid Films* **2005**, 480, 241.
- [109] M. Gloeckler, I. Sankin, Z. Zhao, *IEEE J. Photovoltaics* **2013**, 3, 1389.
- [110] X. Zhao, H. Shen, Y. Zhang, X. Li, X. Zhao, M. Tai, J. Li, J. Li, X. Li, H. Lin, *ACS Appl. Mater. Interfaces* **2016**, 8, 7826.
- [111] M. A. Contreras, B. Egaas, K. Ramanathan, J. Hiltner, A. Swartzlander, F. Hasoon, R. Noufi, *Progr. Photovoltaics: Res. Appl.* **1999**, 7, 311.
- [112] K. Ramanathan, M. A. Contreras, C. L. Perkins, S. Asher, F. S. Hasoon, J. Keane, D. Young, M. Romero, W. Metzger, R. Noufi, J. Ward, A. Duda, *Progr. Photovoltaics: Res. Appl.* **2003**, 11, 225.
- [113] P. Tockhorn, J. Sutter, R. Colom, L. Kegelmann, A. Al-Ashouri, M. Roß, K. Jäger, T. Unold, S. Burger, S. Albrecht, C. Becker, *ACS Photonics* **2020**, 7, 2589.
- [114] M. A. Morsy, K. Saleh, *IEEE Access* **2022**, 10, 44147.
- [115] B. Qi, J. Wang, *J. Mater. Chem.* **2012**, 22, 24315.
- [116] N. K. Elumalai, A. Uddin, *Energy Environ. Sci.* **2016**, 9, 391.
- [117] K. L. Schulte, J. Simon, M. A. Steiner, A. J. Ptak, *Cell Rep. Phys. Sci.* **2023**, 4, 9.
- [118] H. R. Arzbin, A. Ghadimi, *Mater. Sci. Eng.: B* **2019**, 243, 108.
- [119] C.-Y. Hong, M.-M. Hung, T.-T. Yang, Y.-C. Wang, Y.-C. Lin, P. Yu, in *2015 IEEE 42nd Photovoltaic Specialist Conf. (PVSC)*, IEEE, New Orleans, LA **2015**, pp. 1–3.
- [120] G. A. Landis, D. J. Belgiovane, D. A. Scheiman, in *2011 37th IEEE Photovoltaic Specialists Conf.*, IEEE, Seattle, WA **2011**, pp. 001583–001588.
- [121] J. Balenzategui, A. Martí, *Sol. Energy Mater. Sol. Cells* **2006**, 90, 1068.
- [122] H. Helmers, E. Lopez, O. Höhn, D. Lackner, J. Schön, M. Schauerte, M. Schachtner, F. Dimroth, A. W. Bett, *Phys. Status Solidi RRL* **2021**, 15, 2100113.
- [123] S. Eyderman, S. John, *Sci. Rep.* **2016**, 6, 28303.
- [124] A. R. Bowman, M. Anaya, N. C. Greenham, S. D. Stranks, *Phys. Rev. Lett.* **2020**, 125, 067401.
- [125] F. A. Chaudhry, L. Escandell, E. López-Fraguas, R. Vergaz, J. M. Sánchez-Peña, B. Garca-Cámara, *Sci. Rep.* **2022**, 12, 9240.
- [126] M. Wasiak, J. Walczak, M. Motyka, F. Janiak, A. Trajnerowicz, A. Jasik, *Opt. Mater.* **2017**, 64, 137.
- [127] D. Wang, J. Wu, H. Guo, M. Wu, L. Wu, S. Zhang, J. Ao, H. Wang, Y. Zhang, *Sol. RRL* **2021**, 5, 2000391.
- [128] H. L. Skriver, N. Rosengaard, *Phys. Rev. B* **1992**, 46, 7157.
- [129] Y. Gan, X. Bi, Y. Liu, B. Qin, Q. Li, Q. Jiang, P. Mo, *Energies* **2020**, 13, 5907.
- [130] S. Ghosh, S. Porwal, T. Singh, *Optik* **2022**, 256, 168749.
- [131] G. Vaidhyanathan Krishnamurthy, M. Chirumamilla, T. Krekeler, M. Ritter, R. Raudsepp, M. Schieda, T. Klassen, K. Pedersen, A. Y. Petrov, M. Eich, M. Störmer, *Adv. Mater.* **2023**, 35, 2305922.

- [132] H. M. Branz, C. Teplin, P. Stradins, Current Assignee: Alliance for Sustainable Energy LLC **2013**.
- [133] R. Nasrin, M. Hasanuzzaman, N. A. Rahim, *Int. J. Energy Res.* **2018**, 42, 1115.
- [134] E. Ettah, O. Nawabueze, G. Njar, *Int. J. Appl.* **2011**, 1, 4.
- [135] J. Adeeb, A. Farhan, A. Al-Salaymeh, *J. Ecol. Eng.* **2019**, 20, 5.
- [136] Y. P. Varshni, *Physica* **1967**, 34, 149.
- [137] K. P. O'donnell, X. Chen, *Appl. Phys. Lett.* **1991**, 58, 2924.
- [138] I. Vainshtein, A. Zatsepин, V. Kortov, *Phys. Solid State* **1999**, 41, 905.
- [139] T. Yamamura, K. Takagi, in *CS MANTECH Conf.* Indina Wells, CA **2011**.
- [140] I. Repins, M. A. Contreras, B. Egaas, C. DeHart, J. Scharf, C. L. Perkins, B. To, R. Noufi, *Progr. Photovoltaics: Res. Appl.* **2008**, 16, 235.
- [141] S. Benabbas, Z. Rouabah, H. Heriche, N.-E. Chelali, *Afr. J. Sci. Technol. Innovation Dev.* **2016**, 8, 340.
- [142] M. Hadjab, J.-M. Wagner, F. Bouzid, S. Boudour, A. Hadj Larbi, H. Bennacer, M. I. Ziane, M. Saeed, H. Abid, S. Berrah, *Int. J. Modell. Simul.* **2022**, 42, 179.
- [143] M. Boubakeur, A. Aissat, M. B. Arbia, H. Maaref, J.-P. Vilcot, *Superlattices Microstruct.* **2020**, 138, 106377.
- [144] E. H. Ihalane, L. Atourki, H. Kirou, A. Ihlal, K. Bouabid, *Mater. Today: Proc.* **2016**, 3, 2570.
- [145] R. Prasad, A. Das, U. P. Singh, *Appl. Phys. A* **2021**, 127, 140.
- [146] C. Li, H. Luo, H. Gu, H. Li, *Materials* **2022**, 15, 5883.
- [147] N. E. I. Boukortt, S. Patanè, *Optik* **2020**, 218, 165240.
- [148] S. Sharbati, I. Gharibshahian, A. A. Orouji, *Opt. Mater.* **2018**, 75, 216.
- [149] S. R. I. Biplab, M. H. Ali, M. M. A. Moon, M. F. Pervez, M. F. Rahman, J. Hossain, *J. Comput. Electron.* **2020**, 19, 342.
- [150] A. K. Patel, R. Mishra, S. K. Soni, *Micro Nanostruct.* **2022**, 165, 207195.
- [151] Y. Osman, M. Fedawy, M. Abaza, M. H. Aly, *Opt. Quantum Electron.* **2021**, 53, 245.
- [152] A. Ait Abdelkadir, E. Oublal, M. Sahal, B. M. Soucase, A. Kotri, M. Hangoure, N. Kumar, *Silicon* **2023**, 15, 2125.
- [153] R. Zouache, I. Bouchama, O. Saidani, M. A. Ghebouli, M. S. Akhtar, M. Saeed, S. Boudour, L. Lamiri, O. Belgherbi, M. Messaoudi, *Micro Nanostruct.* **2024**, 207812.
- [154] M. Abdolmaleky, F. Shama, *Optik* **2018**, 172, 271.